ACS OMEGA

http://pubs.acs.org/journal/acsodf

Article

Open Circuit Voltage Enhancement and Defect Suppression of Wide-Bandgap $CsPbIBr_2$ Perovskite Solar Cells by Phenylhydrazinium Chloride Incorporation

Waqas Siddique Subhani, Khalil Harrabi,* Abdelkrim Mekki, Abdulaziz Aljalal, Menouer Saidani, Nabeel Aslam, and Feichi Zhou

Cite This: *ACS Omega* 2026, 11, 10545−10553

Read Online

ACCESS | Metrics & More | Article Recommendations | Supporting Information

ABSTRACT: Wide-bandgap (WBG) perovskite solar cells possess huge potential for integration into next-generation heterojunction photovoltaic systems. Conversely, their well-known commercialization is presently hindered by several challenges, including considerable open circuit voltage losses and poor long-term stability. Here, we report phenylhydrazinium chloride (PCl) as an effective dopant in WBG $CsPbIBr_2$ perovskite solar cells, which inhibits halide oxidation and demixing in addition to decreasing defect density, leading to highly crystalline perovskite films. As a result of lower defects, PSCs obtained by PCl WBG $CsPbIBr_2$ achieved a PCE of 10.83%, possessing a V_{oc} of 1.24 and an enhanced stability of more than 300 h. This work may deliver a viable solution toward the fabrication of WBG $CsPbIBr_2$ PSCs sub-cells for tandem solar cells.

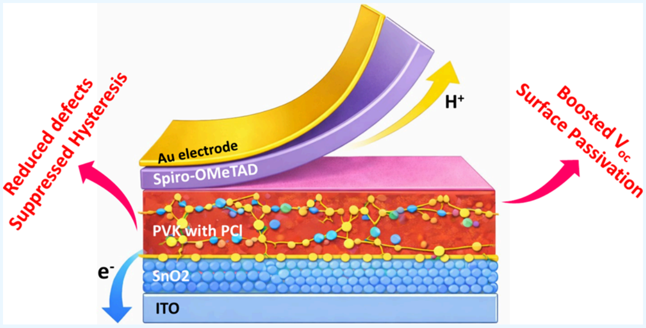

■ INTRODUCTION

Thanks to their easy fabrication route, strong optical absorption, adjustable bandgaps, high charge carrier mobility, and long carrier diffusion lengths, perovskite solar cells (PSCs) have garnered a lot of attention as potential candidates for next-generation photovoltaic technologies.[1−4] Their power conversion efficiencies (PCEs) have surged significantly over the past 10 years, rising from a 3.8% to a current certified efficiency of 27%.[5,6] Considerable studies have been focused on developing wide-bandgap (WBG) perovskite tandem solar cells in order to overcome the efficiency constraints of single-junction PSCs. Development in this area has accelerated, and it is thought to hold great promise for the development of next-generation solar technology. Notably, the overall PCE of perovskite tandem solar cell configurations is largely dependent on the performance of WBG perovskite subcells.[7,8] The development of scalable manufacturing methods for WBG perovskite solar cells that are compatible with ambient-air processing is crucial for assessing the commercialization possibilities for perovskite tandem solar cells. Achieving WBG with high PCE PSCs in ambient circumstances, such as moderate to high humidity, will speed up their transition to commercial viability and drastically lower manufacturing costs. However, a significant obstacle to the large-scale manufacturing and utilization of the state-of-the-art WBG PSCs is that they are mostly made in inert atmospheres.[9]

The overall performance and long-term stability of WBG perovskite solar cells are hampered by photoinduced phase segregation[10,11] and open-circuit voltage (V_{OC}) losses.[12,13] To overcome these constraints, a variety of techniques, like compositional tuning, interfacial modification, additive engineering, and manufacturing process optimization, have been effectively utilized to produce highly efficient WBG PSCs.[14−17] An important strategy that can play a key role in improving the device stability and performance enhancement is doping.[18,19] The optoelectronic device performance of WBG $CsPbIBr_2$ perovskite solar cells was successfully improved by adding sulfamic acid sodium salt (SAS) by Wang et al.[20] The SAS-modified perovskite showed reduced grain boundaries, leading to better stability and higher V_{oc}. Li et al. demonstrated a triacetyl resveratrol (TRES) dopant (acting as an antioxidant additive) in the WBG $CsPbIBr_2$ perovskite precursor to suppress the development of oxidation-driven defects. The resulting devices exhibited a V_{oc} of more than 1.3 V and improved ambient air stability.[21] Yao et al. provided an approach to strain modulation that utilizes alkenamide-terminated $Ti_3C_2T_x$ MXenes in the perovskite precursor solution. In addition to acting as a templating agent to

Received: November 17, 2025
Revised: January 13, 2026
Accepted: January 21, 2026
Published: February 4, 2026

https://doi.org/10.1021/acsomega.5c11624

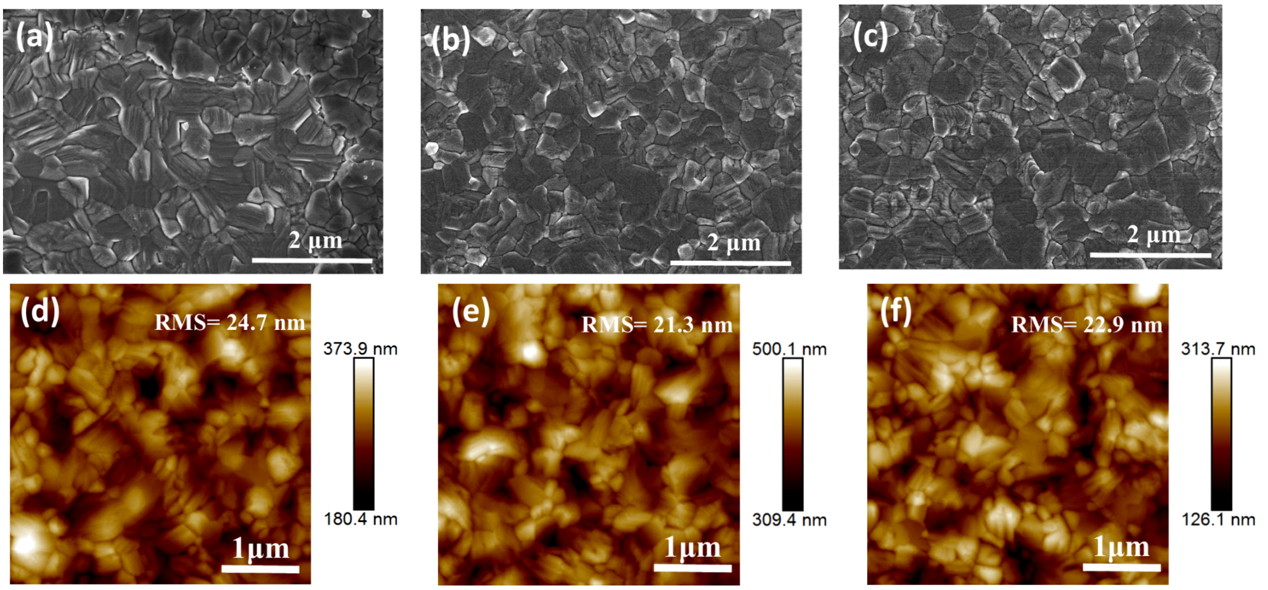

Figure 1. (a) SEM top view micrographs of the $CsPbIBr_2$ films W/O and with (b) 3% PCl (c) 5% PCl. (d) AFM topography (height) image of the $CsPbIBr_2$ films W/O and with (e) 3% PCl and (f) 5% PCl.

promote the creation of high-quality grains, the alkenamides' flexible alkyl chains cause lattice contraction or expansion, which encourages the development of elastic grain boundaries. Within the perovskite layer, this structural modification successfully reduces ion movement channels and regionally distributed strain.[22] Similarly, Zhao et al. examined hydrogen lead triiodide ($HPbI_3$) and cesium acetate (CsAc) as dual additives to modify the structural and optoelectronic characteristics of $CsPbIBr_2$ perovskite solar cells. Co-doping with CsAc and $HPbI_3$ successfully optimized the energy level alignment and passivated trap states inside the $CsPbIBr_2$ films, thus improving device stability, PCE, and V_{oc}.[23] He et al. utilized 1,5-diaminopentane dihydroiodide ($DAPI_2$) on the $CsPbIBr_2$ perovskite layer and suggested it as an efficient surface doping technique. Significantly changed film morphology was observed by this surface modification strategy, which improved the device's overall performance.[24]

Herein, we report phenylhydrazinium chloride (PCl) as an effective dopant in WBG $CsPbIBr_2$ perovskite solar cells with a band gap of 2.1 eV. In addition to successfully passivating interfacial defects, the strong interaction between PCl and $PbBr_2$ was observed to slow down the perovskite crystallization process. The construction of superior quality perovskite films with a lower defect density was made easier by this double impact. As a result of the PCl doping strategy, we achieved a PCE of 10.83% with an improved ambient stability.

■ EXPERIMENTAL DETAILS

Materials

Unless stated otherwise, all chemicals and solvents were purchased commercially and used as received. Chlorobenzene (CB, >99.8%), dimethyl sulfoxide (DMSO 99.99% purity), acetonitrile, 4-*tert*-butylpyridine (4-tBP > 96%), lead bromide ($PbBr_2$ 99.99% purity), cesium iodide (CsI), phenyl-C61-butyric acid methyl ester (PCBM), phenylhydrazinium chloride (PCl), and Au were obtained from Sigma-Aldrich, and tris (2-(1H-pyrazol-1-yl)-4-*tert*-butylpyridine)-cobalt(III) tris (bis(trifluoromethylsulfonyl) imide) (FK 209 CO > 99%) and lithium bis(trifluoromethanesulfonyl)imide (LiTFSI, >99%) were obtained from Sigma-Aldrich. The SnO_2 colloid solution (tin(IV) oxide) was obtained from Alfa Aesar, and 2,2′,7,7′-tetrakis (*N*,*N*-di-*p*-methoxyphenylamine)-9,9′-spirobifluorene (Spiro-OMeTAD, >99.5%) was acquired from Ossila.

Device Fabrication

Hellmanex III detergent, ethanol, IPA, and deionized water were used in succession to clean commercially available ITO glass (sheet resistance ∼ 15 Ω sq^{-1}). UVO ozone was applied to cleaned ITO glass before the spin-coating of the electron transport layer. DI water was used to dilute the 15% SnO_2 colloidal suspension to a 5% concentration. After being prepared, the SnO_2 films were annealed for 30 min at 100 °C and then for 30 min at 150 °C. SnO_2-coated substrates were moved to a glovebox filled with nitrogen (N_2) following treatment with UVO ozone. Equimolar (1.2 M) CsI and $PbBr_2$ were dissolved in DMSO to prepare the $CsPbIBr_2$ precursor solution. The precursor solution was stirred at 70 °C for 4−6 h and filtered with 0.45 mm PTFE filters. For the fabrication of PCl-doped perovskite films, 3 and 5% PCl were added to perovskite precursor films. 80 μL of $CsPbIBr_2$ solution was spin-coated onto the SnO_2 surface at 1000 rpm for 10 s and 4000 rpm for 40 s. As-prepared $CsPbIBr_2$ films were annealed in two steps at 70 °C for 5 min, followed by 180 °C for 20 min. Spiro-OMeTAD was dissolved in chlorobenzene with a concentration of 72 mg/mL, and then 18 μL of lithiumbis(trifluoromethanesulfonyl)imide (520 mg/mL in acetonitrile), 28 μL of 4-*tert*-butylpyridine (tBP), and 10 μL of Co FK209 were added to the solution. The Spiro-OMeTAD solution was spin-coated onto the $CsPbIBr_2$ film at 5000 rpm for 30 s. Finally, 120 nm gold (Au) was deposited by thermal evaporation under a pressure of 5×10^{-4} Torr.

Characterizations

The UV−vis absorption spectra were recorded by a UV−vis spectrophotometer (Jasco V-670). The morphology and crystallization of PSCs were observed with SEM (JEOL, JSM6610LV) and XRD (Rigaku, Ultima). AFM images were obtained using the tapping mode of Veeco Innova diSPM. The XPS measurement was conducted with an X-ray photoelectron spectrometer (Thermo Scientific ESCALAB 250Xi), which used the C 1s peak at 284.5 eV for standard. *I*−*V* characteristics of PSCs were measured under AM 1.5 G illumination at 100 mW cm^{-2} (Newport Thermal 91 192) by using a Keithley 2400 source meter. A Newport quantum efficiency measuring system was used to examine the PSC's external quantum efficiency (EQE) spectra. A DeltaFlex modular fluorescence lifetime system from Horiba Scientific was used for time-resolved photoluminescence spectroscopy. The Mott−Schottky and EIS analyses

https://doi.org/10.1021/acsomega.5c11624
ACS Omega 2026, 11, 10545−10553

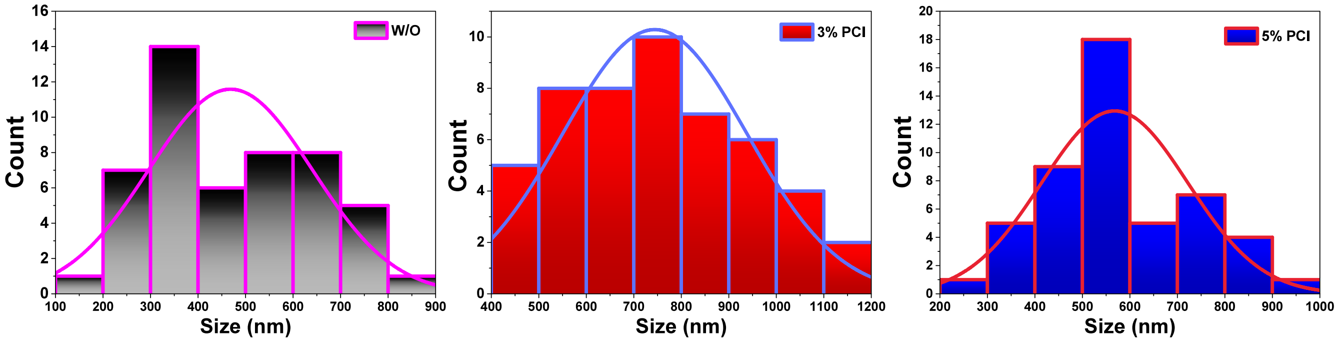

Figure 2. Average grain size distribution obtained from SEM images.

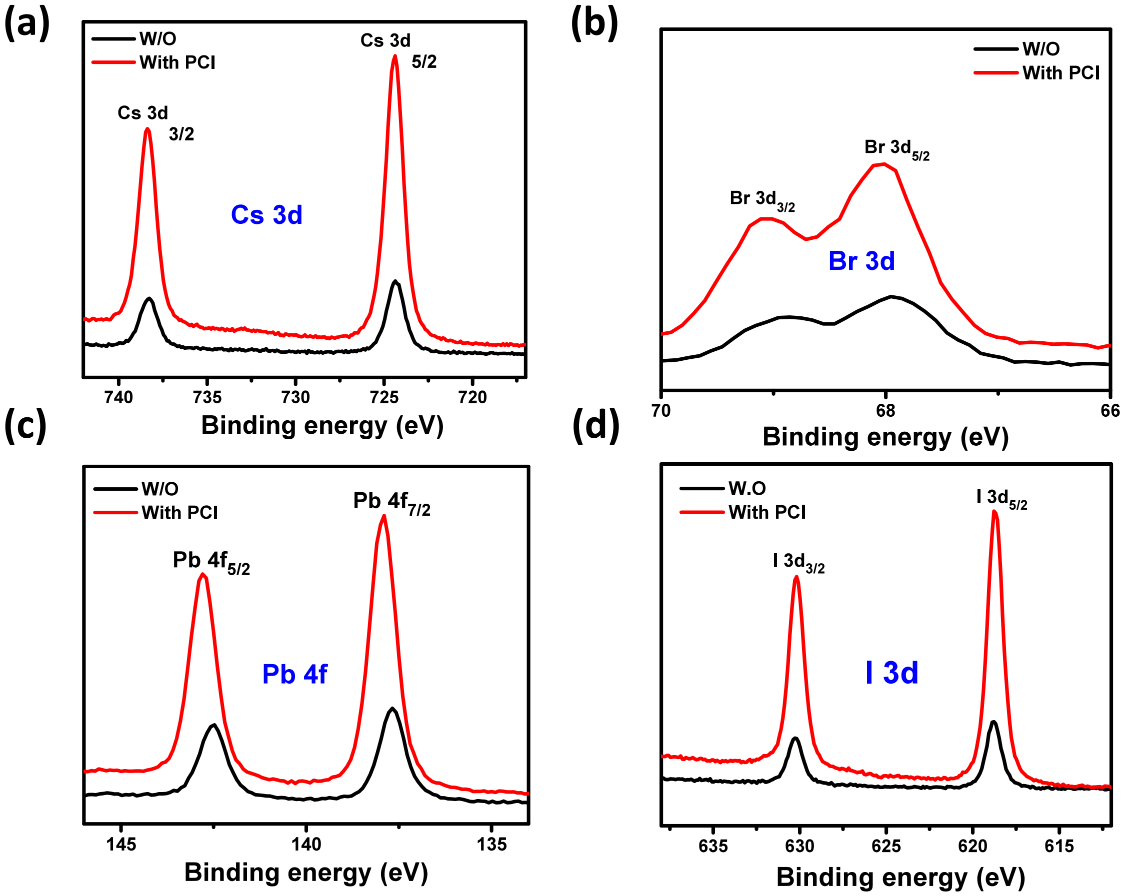

Figure 3. XPS plots of (a) Cs 3d orbital, (b) Br 3d orbital, (c) Pb 4f orbital, and (d) I 3d orbital of the CsPbIBr2 absorber films with the introduction of PCl.

were performed using a Potentiostat (Biologic Science Instruments, VMP3-SAS).

RESULTS AND DISCUSSION

The performance of solar cells is strongly influenced by the coverage and morphology of the perovskite active layer. Top-view SEM images of $CsPbIBr_2$ films prepared with and without PCl are shown in Figure 1a−c. Although the $CsPbIBr_2$ sample W/O PCl incorporation exhibits good surface coverage, there are still some uncovered surface defects due to the heterogeneous nucleation. These defects could act as a recombination center, which will not only degrade the device performance but also initiate the device degradation, leading to a meager lifetime. The surface coverage and morphology were improved significantly upon the introduction of PCl. Compared to the W/O $CsPbIBr_2$ film, the PCl incorporated films show a smoother and denser surface. PCl incorporated films exhibit fewer grain boundaries and large grain size compared to W/O PCl. The average grain size was enhanced from 468.4 nm for W/O to 744 and 568 nm for 3 and 5% PCl doped films, respectively. In addition, the grain boundaries of $CsPbIBr_2$ with 3% PCl are indistinct and highly packed relative to its counterparts, probably owing to the passivation effect of PCl. The average grain size distribution is shown in Figure 2.

Atomic force microscopy (AFM) micrographs of $CsPbIBr_2$ with and W/O PCl are displayed in Figure 1d−f. The root-mean-square roughness (RMS) of the $CsPbIBr_2$ perovskite layers with PCl is 21.3 and 22.9 nm for 3 and 5% PCl doping,

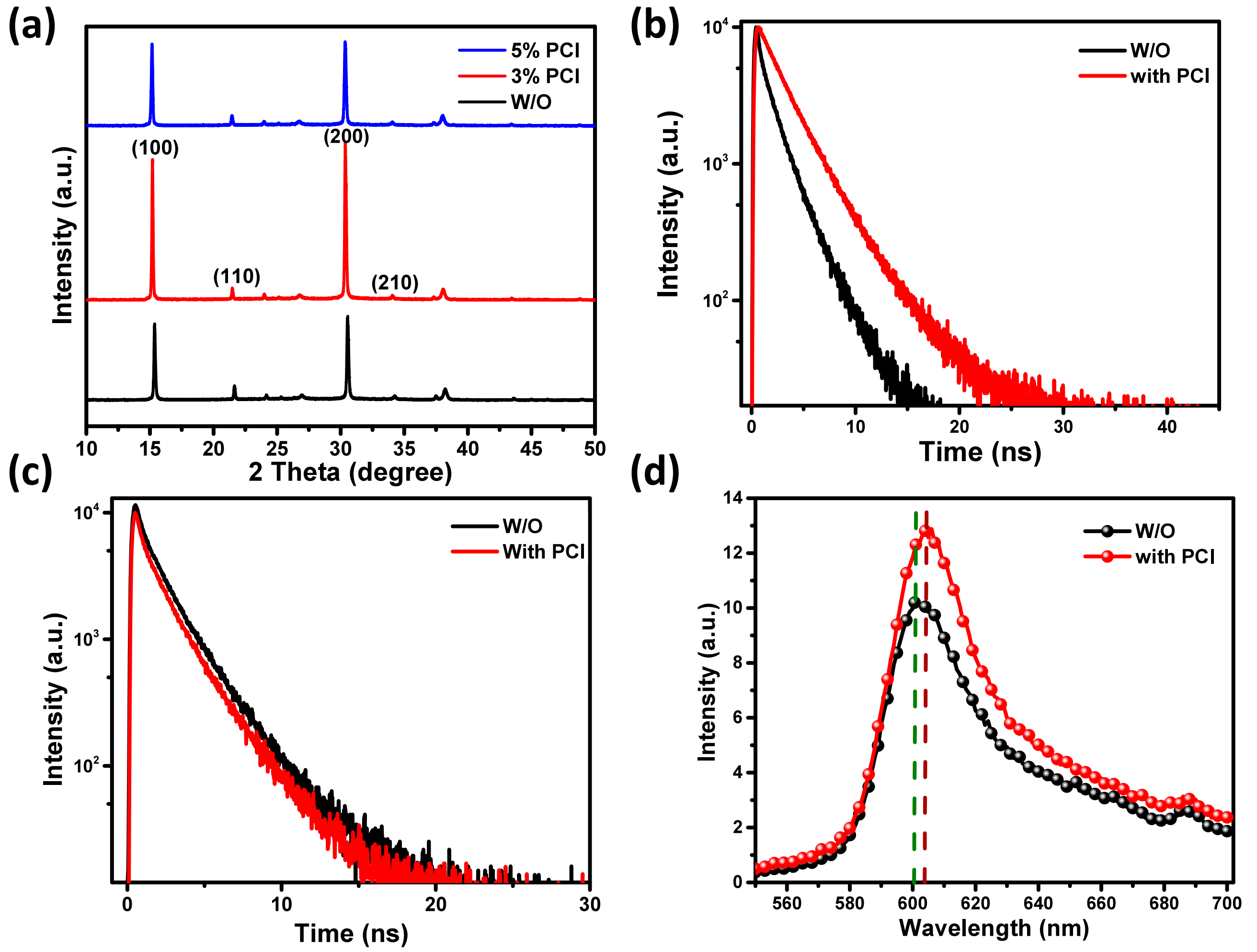

Figure 4. (a) X-ray diffraction (XRD) patterns of $CsPbIBr_2$ absorber films without (W/O) and with PCl incorporation. (b) Time-resolved photoluminescence (TRPL) decay curves of $CsPbIBr_2$ perovskite films deposited on glass substrates without and with PCl incorporation. (c) TRPL decay curves of $CsPbIBr_2$ perovskite films deposited on ITO/SnO_2 substrates without and with PCl incorporation. (d) Steady-state photoluminescence (PL) spectra of $CsPbIBr_2$ perovskite films on glass substrates without and with PCl incorporation.

respectively, which is comparatively lower than that of the W/O sample (24.7 nm). Therefore, the perovskite films with PCl incorporation retain a smoother surface with a low specific surface.

X-ray photoelectron spectroscopy (XPS) was conducted to observe chemical and electronic states, as well as the elemental composition of the resultant films. XPS spectra for Cs 3d, Pb 4f, I 3d, and Br 3d of the $CsPbIBr_2$ films with and W/O PCl are shown in Figure 3. With the introduction of PCl into the $CsPbIBr_2$ absorber films, Pb peaks are slightly shifted toward higher binding energy positions. The perovskite film with 3% PCl incorporation displays two symmetric peaks at ~142.79 and 137.88 eV, which are designated as Pb $4f_{5/2}$ and Pb $4f_{7/2}$. These peak shifts are related to the Pb^{2+} in the perovskite. This binding energy shifting can be described by taking into account the lattice distortion effect and interaction among the neighboring particles that will vary the chemical states upon PCl incorporation. The obtained results point out that as the proportion of PCl/Pb incorporation increases, the peak intensity of PCl increases, which clearly indicates that PCl is effectively doped into the perovskite structure and passivates the defects.[25] Measurement results obtained from XRD and XPS suggest that PCl occupies the interstitial sites in the $CsPbIBr_2$ lattice.

The absorption spectra of the $CsPbIBr_2$ perovskite absorber layers with and W/O varying concentrations of PCl are shown in Figure S1a. All of the films demonstrate nearly identical spectra with an absorption edge around 600 nm, which suggests that a minor extent of PCl incorporation has a small influence on the absorption capability of $CsPbIBr_2$. To estimate the optical bandgaps of $CsPbIBr_2$ perovskites with and W/O PCl doping, we plot $(\alpha h\nu)^2$ as a function of $h\nu$, where α denotes the absorption coefficient and $h\nu$ is the photon energy. The overall optical bandgaps are calculated to be 2.11 eV (Figure S1b), which are in agreement with previous reports.[26,27]

The $CsPbIBr_2$ perovskite films with and without PCl doping were prepared using a direct one-step solution-based spin-coating method, as described in the Experimental Details section. Throughout this work, "W/O" denotes films fabricated without PCl, while "x%-PCl" refers to films containing PCl with concentrations of x = 3% and 5%.

In order to investigate the influence of PCl inclusion on the crystal structure of the $CsPbIBr_2$ films, X-ray diffraction (XRD) measurements were performed, as shown in Figure 4a. All of the perovskite layers demonstrated four different diffraction peaks, which correspond to the (100), (110), (200), and (210) planes of the α-phase $CsPbIBr_2$ perovskite.[18,28] As the PCl

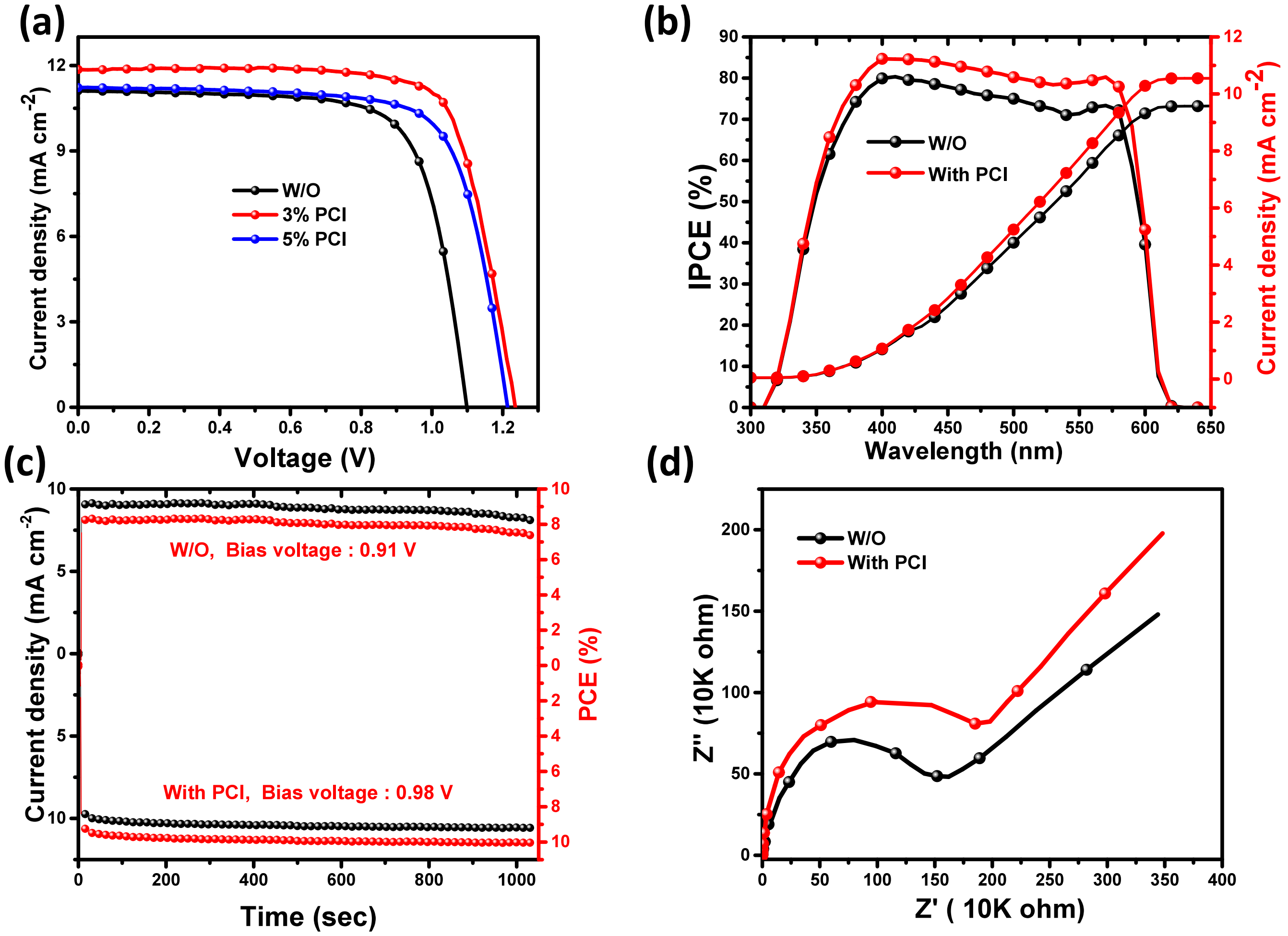

Figure 5. (a) $I-V$ curves of PSCs incorporating PCl under AM 1.5 G (100 mW cm^{-2}) solar irradiation. (b) EQE spectra. (c) Steady-state PCE and current output. (d) Nyquist plots of $CsPbIBr_2$ PSCs incorporating PCl under dark conditions.

content increases in films, the peak position shifts toward a lower 2θ value, which is an indication of lattice expansion of the $CsPbIBr_2$ films upon PCl incorporation.[29] This expansion can be attributed to two main effects associated with PCl incorporation. First, the interaction of the PCl cation with the perovskite lattice, particularly through hydrogen bonding or electrostatic interaction between the $-NH-NH_2^+$ group of PCl and halide ions (I^-/Br^-), can slightly stretch the Pb−X bond lengths, leading to an expanded lattice parameter. Second, the relatively larger ionic radius and organic nature of the PCl molecule may induce local lattice distortion or interfacial strain when partially integrated or adsorbed at the grain surfaces and boundaries.

The corresponding TRPL plot of the perovskite active films on glass is illustrated in Figure 4b, which can be fitted by a biexponential function with an eq[30] 1:

$$f(t) = A_1\exp^{(-t/\tau_1)} + A_2\exp^{(-t/\tau_2)} + K \quad (1)$$

where τ_1 and τ_2 are the fast and slow decay time constants, while A_1 and A_2 are the corresponding decay amplitudes, respectively. It is noteworthy that the PL decay fitting of the glass/perovskite structure is dependent upon the double-exponential function using the fast and slow quenching methods. The aforementioned results are extracted from the surface charge recombination process, whereas the latter is associated with the recombination process taking place at the grains. In order to appropriately estimate the recombination action, the average (t_{ave}) PL decay times is calculated by using t_i and A_i values from the above analysis by applying relation 2:

$$\tau_{ave} = \frac{\sum A_i\tau_i^2}{\sum A_i\tau_i} \qquad i = 1, 2, 3 \ldots \quad (2)$$

As listed in Table S1, t_{ave} increases significantly from 3.39 ns for the 0% PCl to 5.93 ns for the 3% PCl-doped perovskite. The observed lifetime increase is associated with the reduced defect density with blocked non-radiative recombination paths, which is also in good agreement with the steady-state PL. Figure 4c shows the PL of the perovskite film when prepared on the SnO_2 layer. The τ_{ave} are 2.96 and 2.54 ns for the samples W/O and with PCl incorporation, respectively (Table S2). This result validates that the perovskite film with PCl is beneficial for charge carrier collection and extraction. Consequently, the presence of PCl can confine the non-radiative recombination and enhance the charge carrier extraction at the interface of the perovskite. To understand the effect of PCl incorporation on the nonradiative recombination of the perovskite active films on glass, the charge kinetics is explored by using steady state photoluminescence (PL), as shown in Figure 4d. It is observed that there is certainly a gradual rise in steady-state PL intensity with the increment of PCl content, in spite of the film's coverage. The higher the PCl doping inside the perovskite film, the

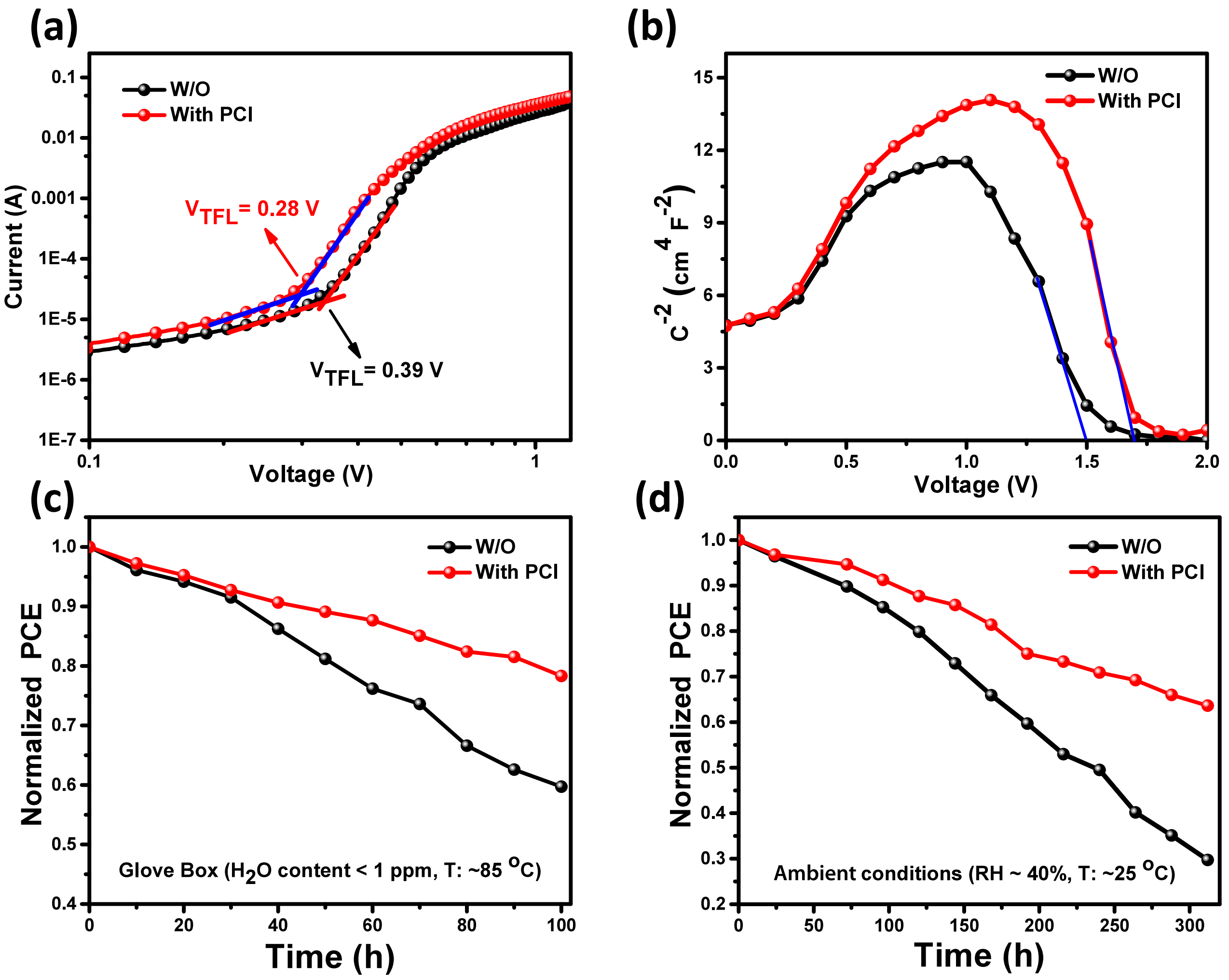

Figure 6. (a) Dark current measurements of CsPbIBr$_2$ PSCs with and W/O PCl. (b) Mott−Schottky analysis of CsPbIBr$_2$ PSCs with and W/o PCl. (c) operational stability of nonencapsulated PSCs at 85 °C in a N$_2$ environment. (d) Operational stability of nonencapsulated PSCs at 25 °C in an ambient environment.

higher the intensity of PL. It is a known fact that the higher PL intensity is linked with fewer defects and trap states in the perovskite absorber layer. Therefore, we can deduce that PCl doping considerably reduces the defects and trap states in the perovskite active layer. In addition, there is a slight Red shift in the emission peak identified by the PL emission spectra, as displayed in Figure 4d. The red-shift of ∼4 nm (compared to the W/O 601.32 nm and 3% doped 605.41 nm) might be attributed to the significantly enlarged size of the crystals of the perovskite as reported in the literature.

To inspect the influence of PCl introduction on the photovoltaic performance, we outlined CsPbIBr2 PSCs with different amounts of PCl under AM 1.5 illumination at 100 mW cm^{-2}. The characterized J−V curves are presented in Figure 5a. The champion device parameters are listed in Table S3. Compared to the perovskite solar cells prepared from the undoped condition, the cells from PCl containing precursor attained a higher short circuit current density (J_{SC}), increased from 11.11 to 11.82 mA cm^{-2}. This is mainly attributed to better charge transportation and light absorption. Open circuit voltage (V_{OC}) is significantly influenced by the lower surface defects, reduced recombination at the electron transport interface, and large grain size. The third parameter that helped to increase the power conversion efficiency (PCE) of PSCs is the fill factor (FF). FF was improved due to the restricted series resistance, shunt resistance, and the multiple energy losses at the electrodes. At an optimal PCl concentration of 3%, the champion and average PCE were 10.83 and 10.01% (summarized published results corresponding to Table S4), respectively, which outperformed the W/O sample by 18%. The distribution of photovoltaic parameters obtained from 30 devices is summarized in Figure S2. To further validate the J_{SC}, we observed the incident photon to current conversion efficiency (IPCE), alongside the integrated current density, as shown in Figure 5b. A remarkable external quantum efficiency (EQE) exceeding 80% in the wavelength region of 300−610 nm was attained. The integrated current density calculated from IPCE almost matched the J_{SC}. The small inconsistency could be attributed to the sluggish photovoltaic feedback as well as the spectral disparity between the EQE and the solar simulator source.

Infamous hysteresis is an inherent property related to the perovskites and extremely challenging to completely eradicate in PSCs. The hysteresis is believed to be instigated by deep traps, ion migration, and charge carrier behavior at the interfaces. Particularly, Br-rich perovskites are prone to phase segregation that will cause ion migration, which in succession promotes the construction of charge injection barriers and worsens hysteresis. Hence, reducing the hysteresis in PSCs composed of Br-rich perovskites is extremely important. In this paper, the hysteresis index (HI) is endorsed to quantitatively estimate the hysteresis, while it can be described by the following relation[13] 3:

$$\mathrm{HI} = \frac{\mathrm{PCE}_{\mathrm{reverse}} - \mathrm{PCE}_{\mathrm{forward}}}{\mathrm{PCE}_{\mathrm{reverse}}} \tag{3}$$

where $\mathrm{PCE}_{\mathrm{RS}}$ and $\mathrm{PCE}_{\mathrm{FS}}$ are the PCE observed under reverse and forward scan directions, respectively, as displayed in Figure S3. The HI for the PSC with 3% PCl is reduced to 6% from 22% compared to the W/O one (Table S5). We presumed that alleviated hysteresis is the outcome of controlled ion migration and passivated trap states. The steady output of PSCs was observed at a bias voltage of 0.91and 0.98 V, as shown in Figure 5c. Strikingly, PSC with PCl doping provided a constant J_{SC} above 10 mA cm^{-2}, corresponding to a steady PCE of 10% for a period of 1000 s at ambient conditions, demonstrating that PCl-based devices are extremely stable.

Figure S4 illustrates the variation of VOC as a function of light intensity (III), which can be well described by the following relationship:

$$\mathrm{VOC} = nk_{\mathrm{B}}T/q\ln(I) + C \tag{4}$$

where n is the diode ideality factor, k_{B} is the Boltzmann constant, T is the absolute temperature, q is the elementary charge, and C is a constant. The extracted ideality factor provides direct insight into the dominant recombination mechanisms within the device: values of $n > 1$ indicate a significant contribution from trap-assisted Shockley Read Hall (SRH) recombination, while values approaching unity reflect reduced monomolecular recombination losses.

From the linear fits shown in Figure S4, the ideality factors for the PCl-doped and pristine devices are determined to be 1.44 and 1.83, respectively. The substantially lower ideality factor for the PCl-doped devices clearly indicates a marked suppression of trap-assisted nonradiative recombination. These results provide strong quantitative evidence supporting our conclusion that PCl incorporation effectively reduces defect-mediated recombination pathways, thereby contributing to the enhanced V_{OC} observed in PCl-based perovskite solar cells.

For the sake of a better understanding of the origin of enhanced device performance, electrochemical measurements were conducted. Figure 5d exhibits the electrochemical impedance spectroscopy (EIS) Nyquist plots obtained from the devices with and W/O PCl doping carried out under dark conditions at a bias voltage of 0.5 V. The equivalent circuit model is shown in Figure S5. Here, R_{s} symbolizes the series resistance associated with the wire and contact, C_{g} is the geometric capacitance related to bulk properties of the perovskite, and R_1 and R_2 are considered to be linked with the recombination resistance and give rise to the recombination rate. C_{s} is the surface charge accumulation capacitance at the perovskite interface and the contact. According to the literature, the recombination rate is inversely proportional to the R_{rec}.[31,32] The fitted results are listed in Table S6. R_{rec} increases from 1.30 to 1.85 MΩ after PCl doping, demonstrating that the recombination at the perovskite and the ETL interface has been reduced. The R_{rec} of the PCl-doped device is significantly higher than that of the W/O device at the identical applied voltage, which suggests the reduced charge leakage and compact surface defect that improved the carrier mobility in the PCl-based device, leading to considerably enhanced FF and V_{OC}.

As revealed earlier, morphology and optimized crystallization may help to attain outstanding physical properties of the perovskite films. To precisely evaluate the trap state density, we prepared perovskite solar cells with an electron-only structure of ITO/$\mathrm{SnO_2}$/PVK/PCBM (pheyl-C61-butyric acid methyl ester)/Ag (Figure S6) and tested it under dark conditions. According to the space-charge-limited current model, as shown in Figure 6a, the linear voltage connection at the low bias correlates to the ohmic response. With the increase in bias voltage up to the kink point, the relationship turns out to be quadratic. The kink point between these two regions is called the trap-filled limit voltage (V_{TFL}), which defines the trap state density according to relation[33] 5.

$$n_{\mathrm{t}} = \frac{2V_{\mathrm{TFL}}\varepsilon\varepsilon_o}{eL^2} \tag{5}$$

where L is the perovskite film thickness, ε is the dielectric constant, ε_0 denotes the vacuum permittivity, and e is the elementary charge on an electron. The estimated trap densities for the W/O and PCl-doped perovskite films are 5.92×10^{16} and $3.80 \times 10^{16}\mathrm{cm}^{-3}$, respectively (Table S7). The lower current density of the W/O $\mathrm{CsPbIBr_2}$ device arises from a higher trap density and poorer charge transport, whereas the PCI-modified film shows enhanced current density due to trap passivation and improved carrier mobility via Pb−N and Pb−Cl coordination. Thus, PCl incorporation can alleviate the trap state density and improve the device performance.

Mott−Schottky analysis was done to explore the built-in potential and eventually describe the increase in the V_{OC}. Under the dark conditions, a reverse bias was introduced to overcome the state of balance amid the Fermi levels. The built-in potential (V_{bi}) and interface capacitance at heterojunctions were changed simultaneously conferring to the subsequent Mott−Schottky relation[34] 6:

$$\frac{1}{C^2} = \frac{2}{e\varepsilon\varepsilon_0 N_{\mathrm{D}}}\left(V_{\mathrm{bi}} - V - \frac{kT}{e}\right) \tag{6}$$

where C is the space charge region capacitance, V is the applied voltage, V_{bi} is the built-in potential, k signifies Boltzmann's constant, T is the absolute temperature, and N_{D} is the donor density. As illustrated in Figure 6b, the intercept of the Mott−Schottky curve with the x-axis is the value of the built-in potential. Obviously, the V_{bi} for the device with PCl lies at 1.71 V, which is 210 mV superior to that of the W/O sample (1.50 V). A large V_{bi} not only escalates the driving force for separating photogenerated charge carriers but also helps the creation of an expanded depletion region to effectively suppress the recombination.[35,36]

To determine the stability of $\mathrm{CsPbIBr_2}$ PSCs with and W/O PCl under different operational environments, nonencapsulated PSCs were aged under ambient conditions at a relative humidity of 40−45%, as shown in Figure 6d, and at 85 °C in a $\mathrm{N_2}$ environment. The PCl-based PSCs sustained over 65% of their initial efficiencies after 300 h under an ambient atmosphere, whereas the PSCs W/O PCl degraded at a faster rate and maintained only 30% at the same period of time. The lifetime of the PCl-doped device is 2 times longer than that of the undoped device. Furthermore, the PCl-based device also exhibited higher thermal stability. After aging at 85 °C in a $\mathrm{N_2}$-filled glovebox, 80% of the original efficiency was sustained after 100 h for PCl-based cells, as shown in Figure 6c, whereas W/O PCl devices declined to 60% of the initial PCE after 100 h of constant thermal annealing. These results indicate the better moisture and thermal stability of PCl-based devices as compared to the W/O PCl device. These results are among the best stabilities reported for PSCs with Spiro-OMeTAD as hole transport layers.

CONCLUSIONS

In summary, we employed PCl as an extrinsic dopant material to modify perovskite films to improve the stability and PCE of WBB $CsPbIBr_2$ PSCs. A strong interaction between PCl/Pb was observed that could efficiently suppress the defects in the perovskite active layer and effectively slow down the crystallization process. Non-radiative recombination in the perovskite active layer was reduced marginally. As a result of lower defects, PSCs obtained by PCl WBG $CsPbIBr_2$ achieved a PCE of 10.83%, possessing a V_{oc} of 1.24 and an enhanced stability of more than 300 h. This work may deliver a viable solution toward the fabrication of WBG $CsPbIBr_2$ PSCs sub-cells for tandem solar cells.

ASSOCIATED CONTENT

Supporting Information

The Supporting Information is available free of charge at https://pubs.acs.org/doi/10.1021/acsomega.5c11624.

> UV−vis absorption spectra, distribution of photovoltaic parameters, hysteresis index, VOC as a function of light intensity, equivalent circuit model for EIS fitting, structure of an electron-only device for SCLC measurement, and data about the PL lifetimes, hysteresis index, champion device parameters, summarized published results, EIS fitting, and SCLC-estimated trap densities in a table format (PDF)

AUTHOR INFORMATION

Corresponding Author

Khalil Harrabi − *Interdisciplinary Research Center for Advanced Quantum Computing, King Fahd University of Petroleum and Minerals (KFUPM), Dhahran 31261, Saudi Arabia; Department of Physics, College of Engineering and Physics, King Fahd University of Petroleum and Minerals, Dhahran 31261, Saudi Arabia;* orcid.org/0000-0002-8865-0504; Email: harrabi@kfupm.edu.sa

Authors

Waqas Siddique Subhani − *Interdisciplinary Research Center for Advanced Quantum Computing, King Fahd University of Petroleum and Minerals (KFUPM), Dhahran 31261, Saudi Arabia*

Abdelkrim Mekki − *Department of Physics, College of Engineering and Physics, King Fahd University of Petroleum and Minerals, Dhahran 31261, Saudi Arabia; Interdisciplinary Research Center for Advanced Materials, King Fahd University of Petroleum and Minerals (KFUPM), Dhahran 31261, Saudi Arabia*

Abdulaziz Aljalal − *Department of Physics, College of Engineering and Physics, King Fahd University of Petroleum and Minerals, Dhahran 31261, Saudi Arabia; Interdisciplinary Research Center for Communication Systems and Sensing, King Fahd University of Petroleum and Minerals (KFUPM), Dhahran 31261, Saudi Arabia*

Menouer Saidani − *Nanofabrication Core Lab (NCL), King Abdullah University of Science and Technology (KAUST), Thuwal 23955, Saudi Arabia*

Nabeel Aslam − *Nanofabrication Core Lab (NCL), King Abdullah University of Science and Technology (KAUST), Thuwal 23955, Saudi Arabia*

Feichi Zhou − *School of Microelectronics, Southern University of Science and Technology, Shenzhen 518055, China;* orcid.org/0000-0001-7756-1082

Complete contact information is available at: https://pubs.acs.org/10.1021/acsomega.5c11624

Notes

The authors declare no competing financial interest.

ACKNOWLEDGMENTS

W.S.S. and K.H. gratefully acknowledge the support of the Interdisciplinary Research Center (IRC) for Intelligent Secure Systems, King Fahd University of Petroleum and Minerals, under the research grant # INSS2505.

REFERENCES

(1) Ding, B.; et al. Dopant-additive synergism enhances perovskite solar modules. *Nature* **2024**, *628* (8007), 299−305.

(2) Hartono, N. T. P.; et al. Stability follows efficiency based on the analysis of a large perovskite solar cells ageing dataset. *Nat. Commun.* **2023**, *14* (1), 4869.

(3) Hao, F.; et al. Anomalous Band Gap Behavior in Mixed Sn and Pb Perovskites Enables Broadening of Absorption Spectrum in Solar Cells. *J. Am. Chem. Soc.* **2014**, *136* (22), 8094−8099.

(4) Ma, C.; et al. Solution-Processed Mixed-Dimensional Hybrid Perovskite/Carbon Nanotube Electronics. *ACS Nano* **2020**, *14* (4), 3969−3979.

(5) *Best Research-Cell Efficiencies*; National Renewable Energy Laboratory: Golden, CO, USA. https://www.nrel.gov/pv/interactive-cell-efficiency.html (accessed January 23, 2026).

(6) Kojima, A.; et al. Organometal Halide Perovskites as Visible-Light Sensitizers for Photovoltaic Cells. *J. Am. Chem. Soc.* **2009**, *131* (17), 6050−6051.

(7) Yang, L.; et al. Modulating Binding Strength and Acidity of Benzene-Derivative Ligands Enables Efficient and Hysteresis-Free Perovskite/Silicon Tandem Solar Cells. *Angew. Chem., Int. Ed.* **2025**, *64* (21), No. e202500350.

(8) Liu, J.; et al. Perovskite/silicon tandem solar cells with bilayer interface passivation. *Nature* **2024**, *635* (8039), 596−603.

(9) Li, Z.; et al. Sustainable Molecular Passivation via Heat-Induced Disaggregation and Redox Reactions for Inverted Perovskite Solar Cells. *ACS Energy Lett.* **2024**, *9* (11), 5471−5482.

(10) Xu, J.; et al. Triple-halide wide−band gap perovskites with suppressed phase segregation for efficient tandems. *Science* **2020**, *367* (6482), 1097−1104.

(11) Wang, L.; et al. Strain Modulation for Light-Stable n−i−p Perovskite/Silicon Tandem Solar Cells. *Adv. Mater.* **2022**, *34* (26), No. 2201315.

(12) Jang, W. J.; Jang, H. W.; Kim, S. Y. Recent Advances in Wide Bandgap Perovskite Solar Cells: Focus on Lead-Free Materials for Tandem Structures. *Small Methods* **2024**, *8* (2), No. 2300207.

(13) Li, W.; et al. Phase Segregation Enhanced Ion Movement in Efficient Inorganic CsPbIBr2 Solar Cells. *Adv. Energy Mater.* **2017**, *7* (20), No. 1700946.

(14) Kim, G.; et al. A Thermally Induced Perovskite Crystal Control Strategy for Efficient and Photostable Wide-Bandgap Perovskite Solar Cells. *Solar RRL* **2020**, *4* (6), No. 2000033.

(15) Xia, R.; et al. Interfacial passivation of wide-bandgap perovskite solar cells and tandem solar cells. *J. Mater. Chem. A* **2021**, *9* (38), 21939−21947.

(16) Yu, Y.; et al. Synergetic Regulation of Oriented Crystallization and Interfacial Passivation Enables 19.1% Efficient Wide-Bandgap Perovskite Solar Cells. *Adv. Energy Mater.* **2022**, *12* (33), No. 2201509.

(17) Liu, L.; et al. Self-Assembled Amphiphilic Monolayer for Efficient and Stable Wide-Bandgap Perovskite Solar Cells. *Adv. Energy Mater.* **2023**, *13* (4), No. 2202802.

(18) Zhu, W.; et al. Intermolecular Exchange Boosts Efficiency of Air-Stable, Carbon-Based All-Inorganic Planar CsPbIBr2 Perovskite Solar Cells to Over 9%. *Adv. Energy Mater.* **2018**, *8* (30), No. 1802080.

(19) Zhu, W.; et al. Band Alignment Engineering Towards High Efficiency Carbon-Based Inorganic Planar CsPbIBr2 Perovskite Solar Cells. *ChemSusChem* **2019**, *12* (10), 2318−2325.

(20) Wang, Y.; et al. Extrinsic Ion Distribution Induced Field Effect in CsPbIBr2 Perovskite Solar Cells. *Small* **2020**, *16* (17), No. 1907283.

(21) Li, J.; et al. Air-fabricated CsPbIBr2 perovskite film for efficient and stable solar cells by a triacetyl resveratrol additive. *Chem. Commun.* **2024**, *60* (65), 8617−8620.

(22) Yao, X.; et al. Stretchable alkenamides terminated Ti3C2Tx MXenes to release strain for lattice-stable mixed-halide perovskite solar cells with suppressed halide segregation. *Carbon Energy* **2023**, *5* (12), No. e387.

(23) Zhao, X.; et al. Efficient all-inorganic CsPbIBr2 perovskite solar cells with an open voltage over 1.33 V by dual-additive strategy. *Surfac. Interfac.* **2023**, *40*, No. 103145.

(24) He, J.; et al. Synergistic Effect of Surface p-Doping and Passivation Improves the Efficiency, Stability, and Reduces Lead Leakage in All-Inorganic CsPbIBr2-Based Perovskite Solar Cells. *Small* **2023**, *19* (6), No. 2205962.

(25) Cao, Y.; et al. Buried interface modification for high performance and stable perovskite solar cells. *Energy Environ. Sci.* **2025**, *18* (8), 3659−3667.

(26) Subhani, W. S.; et al. Goldschmidt-rule-deviated perovskite CsPbIBr2by barium substitution for efficient solar cells. *Nano Energy* **2019**, *61*, 165−172.

(27) Jiang, X.; et al. Dual-Interface Modification of CsPbIBr2 Solar Cells with Improved Efficiency and Stability. *Adv. Mater. Interfac.* **2021**, *8* (7), No. 2001994.

(28) Subhani, W. S.; et al. Interface-Modification-Induced Gradient Energy Band for Highly Efficient CsPbIBr2 Perovskite Solar Cells. *Adv. Energy Mater.* **2019**, *9* (21), No. 1803785.

(29) Sun, H.; et al. Pb-Reduced CsPb0.9Zn0.1I2Br Thin Films for Efficient Perovskite Solar Cells. *Adv. Energy Mater.* **2019**, *9* (25), No. 1900896.

(30) Feng, J.; et al. High-throughput large-area vacuum deposition for high-performance formamidine-based perovskite solar cells. *Energy Environ. Sci.* **2021**, *14* (5), 3035−3043.

(31) Almora, O.; et al. Capacitive Dark Currents, Hysteresis, and Electrode Polarization in Lead Halide Perovskite Solar Cells. *J. Phys. Chem. Lett.* **2015**, *6* (9), 1645−1652.

(32) Fu, S.; et al. Efficient Passivation with Lead Pyridine-2-Carboxylic for High-Performance and Stable Perovskite Solar Cells. *Adv. Energy Mater.* **2019**, *9* (35), No. 1901852.

(33) Zhu, X.; et al. Vapor-fumigation for record efficiency two-dimensional perovskite solar cells with superior stability. *Energy Environ. Sci.* **2018**, *11* (12), 3349−3357.

(34) Li, N.; et al. Cation and anion immobilization through chemical bonding enhancement with fluorides for stable halide perovskite solar cells. *Nat. Energy* **2019**, *4* (5), 408−415.

(35) Liu, L.; et al. Fully Printable Mesoscopic Perovskite Solar Cells with Organic Silane Self-Assembled Monolayer. *J. Am. Chem. Soc.* **2015**, *137* (5), 1790−1793.

(36) Laban, W. A.; Etgar, L. Depleted hole conductor-free lead halide iodide heterojunction solar cells. *Energy Environ. Sci.* **2013**, *6* (11), 3249−3253.